Supporting Information

Built-in electrophilic/nucleophilic domain of nitrogen-doped carbon nanofiber confined Ni_2P/Ni_3N nanoparticles for efficient urea-containing water splitting reaction

Jiaxin Li[a,b], Chun Yin[a,c], Shuli Wang[c], Baogang Zhang[b*] and Ligang Feng[a*]

a. Faculty of Materials Science and Engineering, Kunming University of Science and Technology, Kunming 650093, China Email: fenglg11@gmail.com (L Feng).

b. School of Water Resources and Environment, MOE Key Laboratory of Groundwater Circulation and Environmental Evolution, China University of Geosciences (Beijing), Beijing, 100083, P.R. China. Email: baogangzhang@cugb.edu.cn.

c. School of Chemistry and Chemical Engineering, Yangzhou University, Yangzhou 225002, P.R. China.

Experiments:

1. Materials and chemicals

N, N-dimethylformamide (DMF), nickel (II) acetate tetrahydrate ($Ni(Ac)_2 \cdot 4H_2O$), sodium hypophosphite (NaH_2PO_2), urea (CH_4N_2O), and potassium hydroxide (KOH) were purchased from Shanghai Aladdin Biochemical Technology Co., Ltd. Polyacrylonitrile (PAN, Mw=150000) and 5 wt.% Nafion ionomers were obtained from Sigma-Aldrich. Ethanol absolute (C_2H_6O) was bought from Beijing Chemical Works. Ultrapure water (18.2 MΩ, Thermo Fisher Scientific Co., LTD, USA) was used throughout all experiments.

2. Synthetic procedures

2.1 Synthesis of Ni-embedded N-doped carbon nanofiber

0.5 g PAN and 3 mmol $Ni(Ac)_2 \cdot 4H_2O$ were dissolved in 6 mL DMF solvent and magnetically stirred for 12 hours. Afterwards, the obtained solution was transferred into a 10 mL syringe equipped with a 22-gauge stainless-steel needle. The prepared precursor solution was subsequently electrospun under a high voltage of 16 kV at a feeding rate of 0.012 mL min^{-1}. A grounded stainless steel flat plate covered with smooth aluminium foil paper was used as a collector, the distance between the injector nozzle and the receiver was 15 cm. The obtained nanofiber membrane was first pre-oxidized in a muffle furnace at 230 ^oC for 2 h (heating rate: 1 ^oC min^{-1}). Then it was further heated in a tube furnace at 800 ^oC in N_2 for 2 h (heating rate: 2 ^oC min^{-1}) to realize the organic carbonization and metal salt decomposition. Finally, Ni embedded N-doped carbon nanofiber (Ni/NCNF) was obtained.

2.2. Synthesis of Ni_3N, Ni_2P and Ni_2P/Ni_3N embedded N-doped carbon nanofiber

20 mg of Ni/NCNF was placed in a porcelain boat and calcinated in a tube furnace at 400 ^oC for 4 h in NH_3 atmosphere (heating rate: 2 ^oC min^{-1}). After cooling down to room temperature, the solid mixture was washed with ultrapure water and dried in a vacuum oven at 60 ^oC for 10 h. The obtained product was abbreviated as Ni_3N/NCNF.

20 mg of Ni/NCNF and 200 mg of NaH_2PO_2 were fully mixed and placed in the middle of a porcelain boat. The phosphorization process was performed in a tube furnace at 350 ^oC for 2 h in a nitrogen atmosphere (heating rate: 2 ^oC min^{-1}). Once cooled, the solid mixture was washed with ultrapure water and dried in a vacuum oven at 60 ^oC for 10 h. The obtained product was abbreviated as Ni_2P/NCNF.

20 mg Ni_3N/NCNF and 200 mg NaH_2PO_2 were separately placed at both ends of a porcelain boat with NaH_2PO_2 powder at the upstream side. Then, the phosphorization, washing, and drying processes were the same as the above steps. The finally obtained product was designated as Ni_2P/Ni_3N/NCNF.

3. Physical Characterizations

The crystal structures of products were detected by Powder X-ray diffraction (XRD, Bruker D8 advance) patterns using Cu Kα (λ = 1.5405 Å) radiation source operating at 40 kV and 40 mA at a scanning rate of 5^o min^{-1}. The crystal structures of the composite were verified and refined through the Reitveld method using general structure analysis system-II (GSAS-II) software. The background of the XRD pattern was simulated using the function of "Chebyschev-1" with 15 coefficients. The peak profile was modeled by the variation of the pseudo-Voigt function. The morphologies and structural characterizations were investigated by scan electron microscopy (SEM, FEI Sirion-200). Transmission electron microscopy (TEM), high-resolution transmission electron microscopy (HRTEM), high-annular dark-field scanning transmission electron microscopy (STEM) and element mapping analysis were conducted on FEI TECNAI G2 electron microscope operating at 200 kV. The energy-dispersive X-ray (EDX) analysis was performed on KEVEX X-ray energy detector. X-Ray photoelectron spectroscopy (XPS) measurements were carried out on Thermo Scientific ESCALAB 250Xi (USA) with an Al Kα radiation source. A water contact angle was obtained by a drop shape analyzer (POWEREACH JC2000D3). The digital photographs of water droplets on surfaces were obtained by a digital camera.

4. Electrochemical measurements

The data was acquired by the Gamry framework system and fitted through the Echem Analyst software package. The working electrode was prepared as follows: 5 mg of the as-prepared catalysts were dispersed entirely into the mixture of 950 μL ethanol and 50 μL Nafion (5 wt%), after sonication for 30 min to make a homogeneous ink, 10 μL of the catalyst ink was pipetted and dropped onto the pre-cleaned glassy carbon electrode with a geometric surface area of 0.07 cm^2 and dried at room temperature. A graphite rod and a Hg/HgO electrode were employed as counter and reference electrodes, respectively. The accuracy of the reference electrode was carefully checked before and after the tests to ensure precise measurements. All the potentials were converted and referred to a reversible hydrogen electrode (RHE) unless otherwise noted. The current was reported

by normalizing the current to the geometric surface area of the electrode unless otherwise noted.

The UOR and OER measurements were tested in a typical three-electrode system. The catalytic performance was evaluated by cyclic voltammetry (CV) and linear scan voltammetry (LSV). The catalytic performance of samples for OER was evaluated by linear sweep voltammograms (LSV) at a scan rate of 5 mV s^{-1} with the potential range from 1.1 V to 1.7 V vs. RHE in 1 M KOH electrolyte. The catalytic performance of the catalysts for UOR was examined by cyclic voltammetry (CV) with the potential from 1.04 V to 1.54 V vs. RHE at different scan rates of 1, 2, 5, and 10 mV s^{-1} in 1 M KOH with and without 0.33 M urea solution.

The Tafel slope was calculated from the following equation: $\eta = a + b \log(j)$, $b = 2.3*RT/\alpha F$, where η is the overpotential (mV), a represents the intercept, j stands for the current density and b defines the Tafel slope. R, T, α, F refer to gas constant, temperature, charge transfer coefficient, and Faraday constant, respectively. α can reflect the intrinsic property of electron transfer; the larger the value, the better the electrochemical dynamics.[1]

The electrochemical impedance spectroscopy (EIS) was recorded in the above three-electrode cell at the frequency ranging from 1000 kHz to 10 mHz with 12 points per decade. The sinus amplitude potential signal was 5 mV. The obtained curves were analyzed and fitted by ZsimpWin computer program.

The chronoamperometry (CA) of UOR and OER was tested at 1.40 and 1.52 V vs RHE, respectively.

The electrochemical surface area (ECSA) was calculated by using the charge required to reduce NiOOH to $Ni(OH)_2$ in the backward scan of CV curves in KOH solution according to the formula [2, 3]: ECSA=Q/0.257*m, in which the charge (Q) represented the cathodic reduction peak of Ni^{3+}/Ni^{2+}. The Q=peak area (S)/scan rate (v), where S was estimated via integrating the area of the reduction peak of the CV diagram. The 0.257 mC cm^{-2} is the charge required to form a monolayer of Ni^{2+}, and m is the loading amount of the catalyst. The intrinsic activity of all the catalysts was revealed by normalizing the current to the ESA to evaluate the catalytic efficiency of the active sites. In addition, the ECSA was also calculated via the double layer capacitance (C_{dl}) by measuring CV curves at various scan rates (10, 20, 40, 60, 80, 100 mV s^{-1}) in a non-Faradaic region. The ECSA can be calculated through the following equation, $ECSA=C_{dl}/C_s$, where C_s is the specific capacitance for a smooth and plain electrode (0.04 mF cm^{-2}) [4].

The Faradaic efficiency of OER was obtained in a gas-tight electrochemical cell coupling with a gas burette. The working electrode was prepared by drop-casting catalyst suspension on the glassy carbon electrode with a surface area of 0.07 cm^2. The potential needed for achieving the benchmark current density of 10 mA cm^{-2} was applied to the electrode and the volume of the evolved gas was recorded synchronously. Thus, the faradaic yield was calculated from the ratio of the recorded gas volume to the theoretical gas volume during the charge passed through the electrode [5].

$$\text{Faradaic yield} = \frac{V_{experimental}}{V_{theoretical}} = \frac{V_{experimental}}{\frac{1}{4} \times \frac{Q}{F} \times V_m}$$

where Q is the charge passed through the electrode, F is Faraday constant (96485 C mol^{-1}), the number 4 means 4 mole electrons per mole O_2, the number 1 means 1 mole O_2, V_m is molar volume of gas (24.5 L mol^{-1}, 298 K, 101 KPa).

The Faradaic efficiency of UOR was obtained by measuring the electron numbers consumed by N_2 via the following equation.

$$FE(\%) = \frac{6 \times n \times F}{Q} \times 100\%$$

Where 6 is the electron transfer number in UOR, n is the amount of N_2 produced (mol), F is the Faraday constant (96485 C mol^{-1}), and Q is the total charge passed (C).

$$FE(\%) = \frac{6 \times \frac{0.95 \times 0.001}{22.4} \times 96485}{102.48 \times 3600 \times 0.07 * 0.001} \times 100\% = 95.07\%$$

The TOF values for UOR were calculated from the following equation:

$$TOF = \frac{J \times A}{F \times 6 \times x}$$

where J is the current density (A m^{-2}), A is the surface area of the electrode (m^2), F is the Faraday constant (96485.3 C mol^{-1}), x is the number of moles of active materials that are deposited onto the electrode.

$$TOF_{Ni_2P/Ni_3N} = \frac{0.001 \times 151.11 \times 0.07}{96485.3 \times 6 \times (\frac{0.001 \times 0.05 \times 79.8\%}{149} \times 2 + \frac{0.001 \times 0.05 \times 20.2\%}{191} \times 3)} = 0.026\ s^{-1}$$

$$TOF_{Ni_2P} = \frac{0.001 \times 82.57 \times 0.07}{96485.3 \times 6 \times (\frac{0.001 \times 0.05 \times \frac{59 \times 2}{149}}{59})} = 0.015\ s^{-1}$$

$$TOF_{Ni_3N} = \frac{0.001 \times 50.66 \times 0.07}{96485.3 \times 6 \times \left(\frac{0.001 \times 0.05 \times \frac{59 \times 3}{149}}{59}\right)} = 0.008\ s^{-1}$$

$$TOF_{Ni} = \frac{0.001 \times 35.48 \times 0.07}{96485.3 \times 6 \times \left(\frac{0.001 \times 0.05 \times \frac{59}{59}}{59}\right)} = 0.005\ s^{-1}$$

Overall water splitting and urea electrolysis tests were measured in a two-electrode system with the Ni_2P/Ni_3N/NCNF catalyst as anode and commercial Pt/C catalyst as cathode. The CV curves were tested in the absence and presence of 0.33 M urea in 1 M KOH at a scan rate of 5 mV s^{-1} with the potential range from 1.0 to 1.8 V. The CA test of overall water splitting and urea electrolysis were all conducted at 1.6 V for 10 h.

5. Calculation method

We have employed the VASP [6, 7] to perform all the density functional theory (DFT) calculations within the generalized gradient approximation (GGA) using the Perdew-Burke-Ernzerhof (PBE) formulation [8]. We have chosen the projected augmented wave (PAW) potentials to describe the ionic cores [9]. Take valence electrons into account using a plane wave basis set with a kinetic energy cutoff of 450 eV. Partial occupancies of the Kohn-Sham orbitals were allowed using the Gaussian smearing method and a width of 0.05 eV. The electronic energy was considered self-consistent when the energy change was smaller than 10^{-5} eV. A geometry optimization was considered convergent when the energy change was smaller than 0.05 eV/Å. The Brillourin zone was sampled with a gamma-centered grid 4×2×1 for all processes [10].

We construct a Ni_3N (110) surface model (model 1) with p (2x2) periodicity in the x and y directions and 3 stoichiometric layers in the z direction separated by a vacuum layer in the depth of 16 Å to separate the surface slab from its periodic duplicates. Model 1 comprises 72 Ni and 24 N atoms. During structural optimizations, a 4×2×1 k-point grid in the Brillouin zone was used for k-point sampling, and the bottom stoichiometric layer was fixed while the top one was allowed to relax.

We then use it to construct a Ni_2P (210) surface model (model 2) with p (2×1) periodicity in the x and y directions and 4 stoichiometric layers in the z direction separated by a vacuum layer in the depth of 16 Å to separate the surface slab from its periodic duplicates. Model 2 comprises 48 Ni

and 24 P atoms. During structural optimizations, a 4×2×1 k-point grid in the Brillouin zone was used for k-point sampling, and the bottom stoichiometric layer was fixed while the top one was allowed to relax.

In model 3, a Ni_3N (110) and Ni_2P (210) surface were built heterojunction; During structural optimizations, a 4×2×1 k-point grid in the Brillouin zone was used for k-point sampling, and the bottom stoichiometric layer was fixed while the rest of all atoms were allowed to relax.

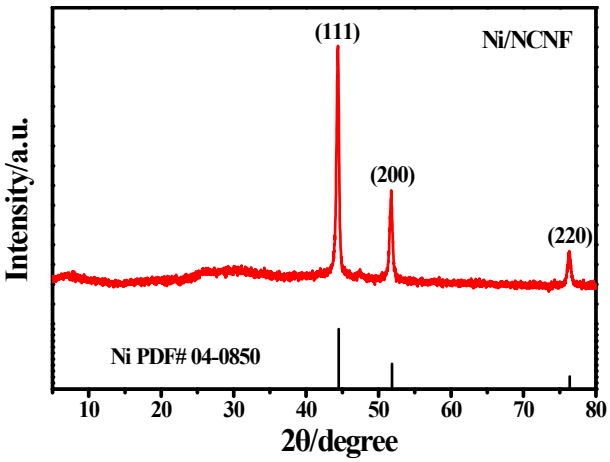

Fig. S1. XRD pattern of Ni/NCNF.

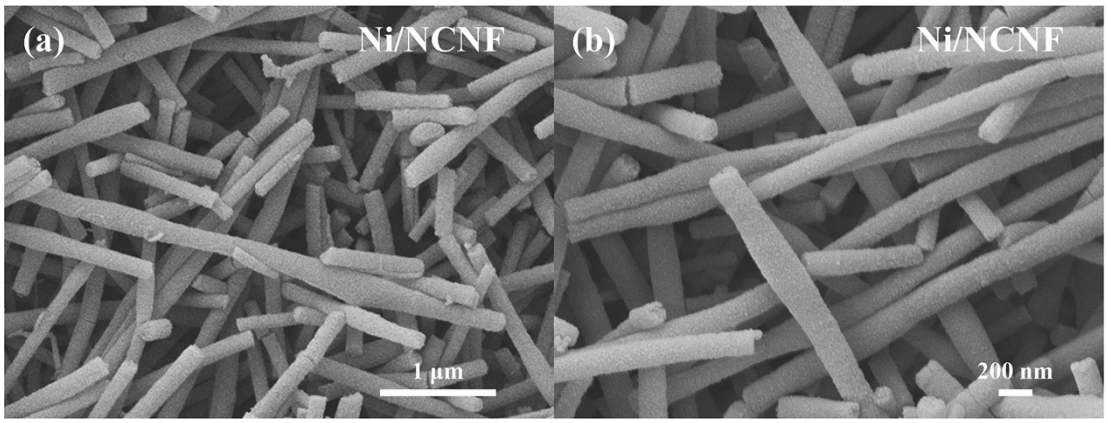

Fig. S2. SEM images of Ni/NCNF at different magnification.

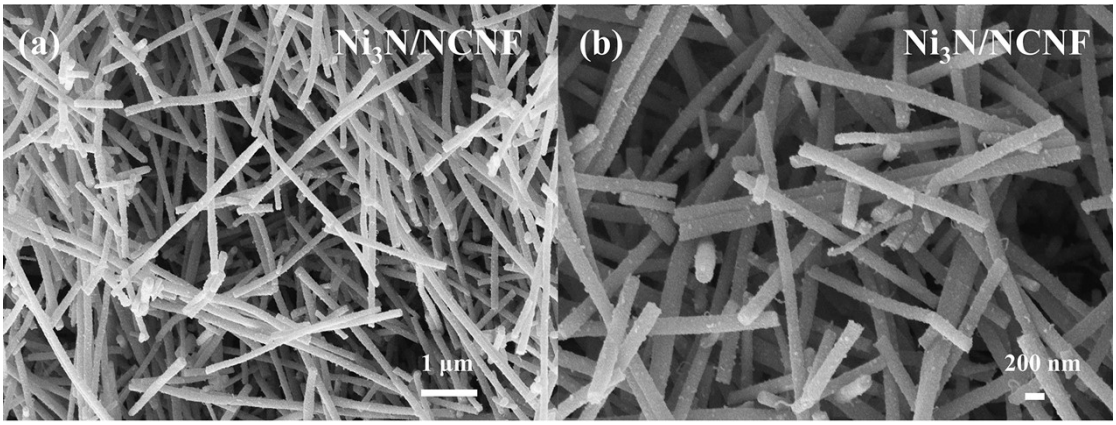

Fig. S3. SEM images of Ni_3N/NCNF at different magnification

.

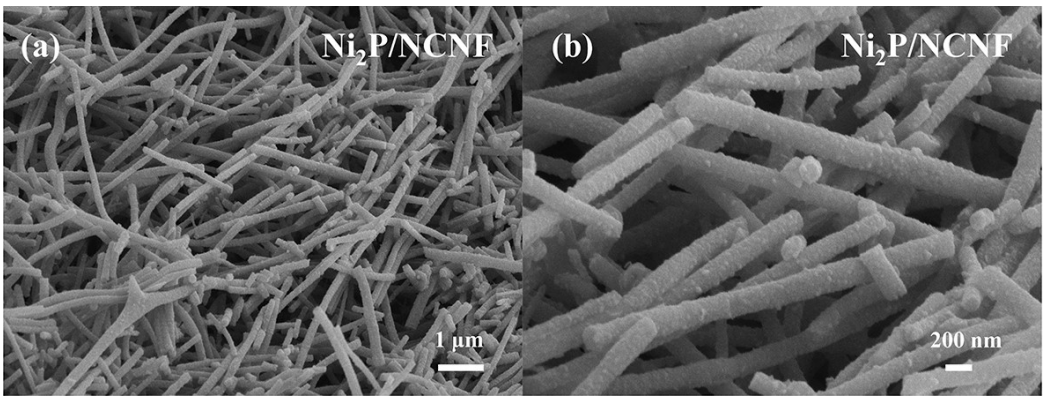

Fig. S4. SEM images of Ni_2P/NCNF at different magnification.

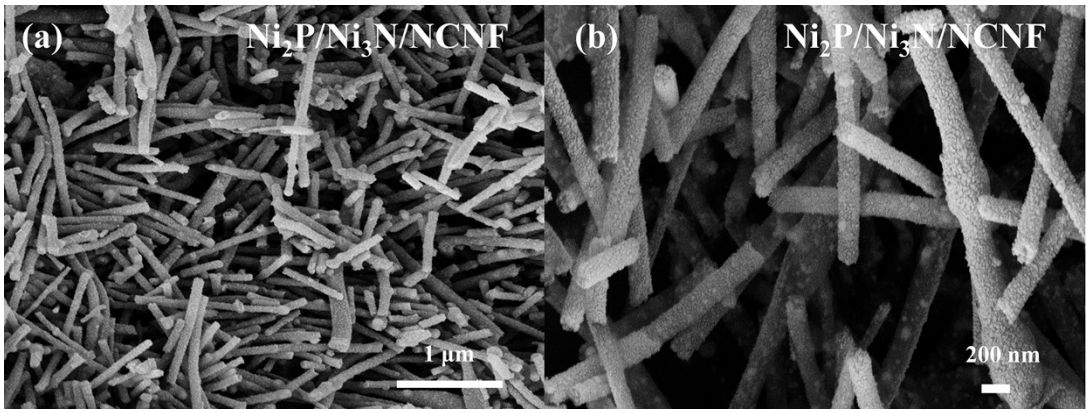

Fig. S5. SEM images of Ni_2P/Ni_3N/NCNF at different magnification.

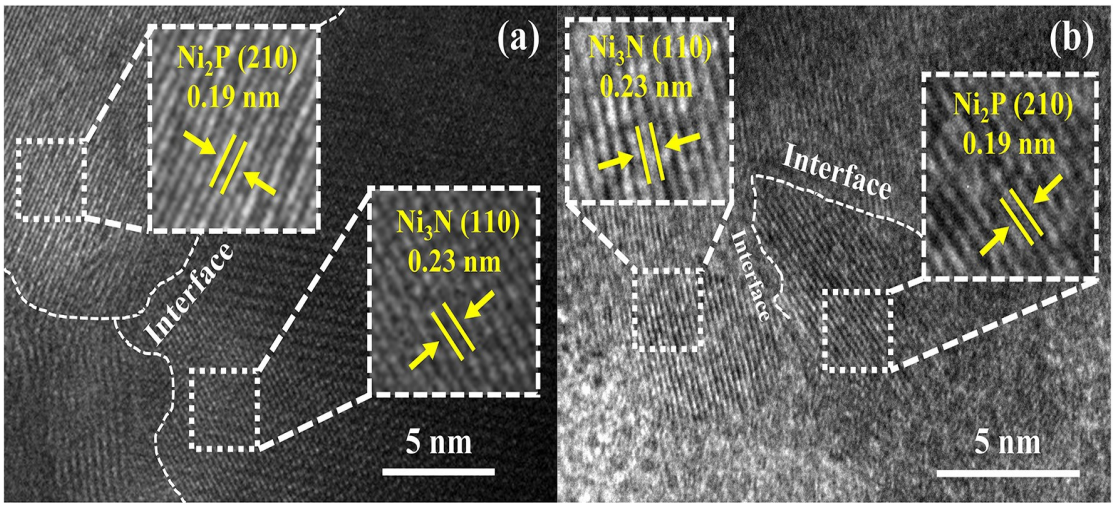

Fig. S6. HRTEM images of Ni_2P/Ni_3N/NCNF.

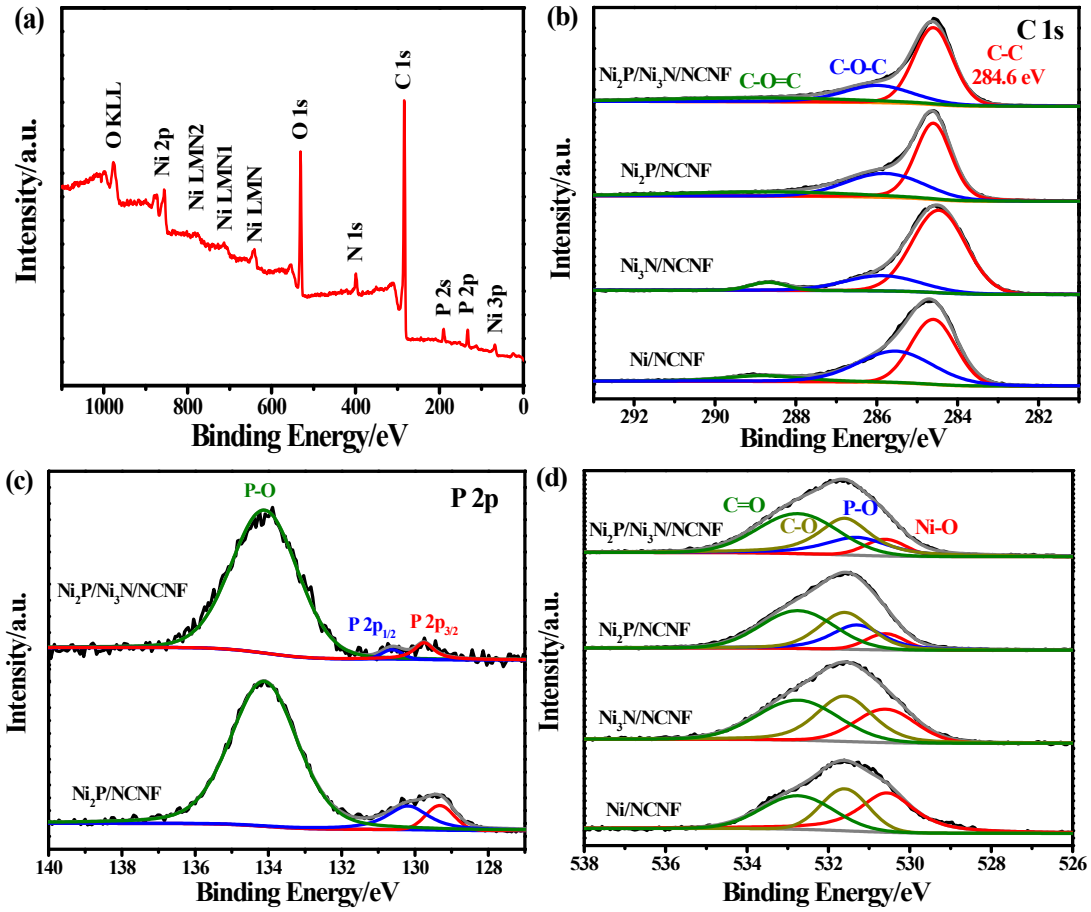

Fig. S7. (a) XPS survey spectrum of $Ni_2P/Ni_3N/NCNF$. XPS spectra of (b) C 1s, (c) P 2p, and (d) O 1s region for Ni/NCNF, $Ni_3N/NCNF$, $Ni_2P/NCNF$, and $Ni_2P/Ni_3N/NCNF$.

Fig. S8. The equivalent circuit used in EIS fitting for OER.

R_s is a sign of the uncompensated solution resistance, CPE is a constant phase element, R_{ct} reflects the charge-transfer resistance.

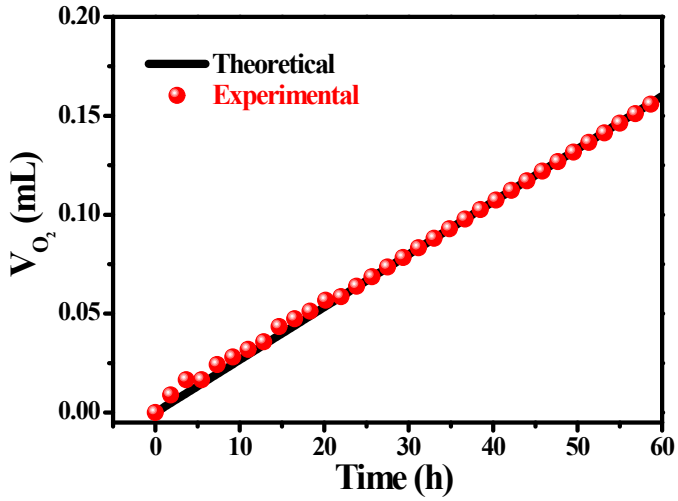

Fig. S9. The current efficiency of Ni_2P/Ni_3N/NCNF for OER by comparing the experimental and theoretical O_2 volumes as a function of oxygen evolution time.

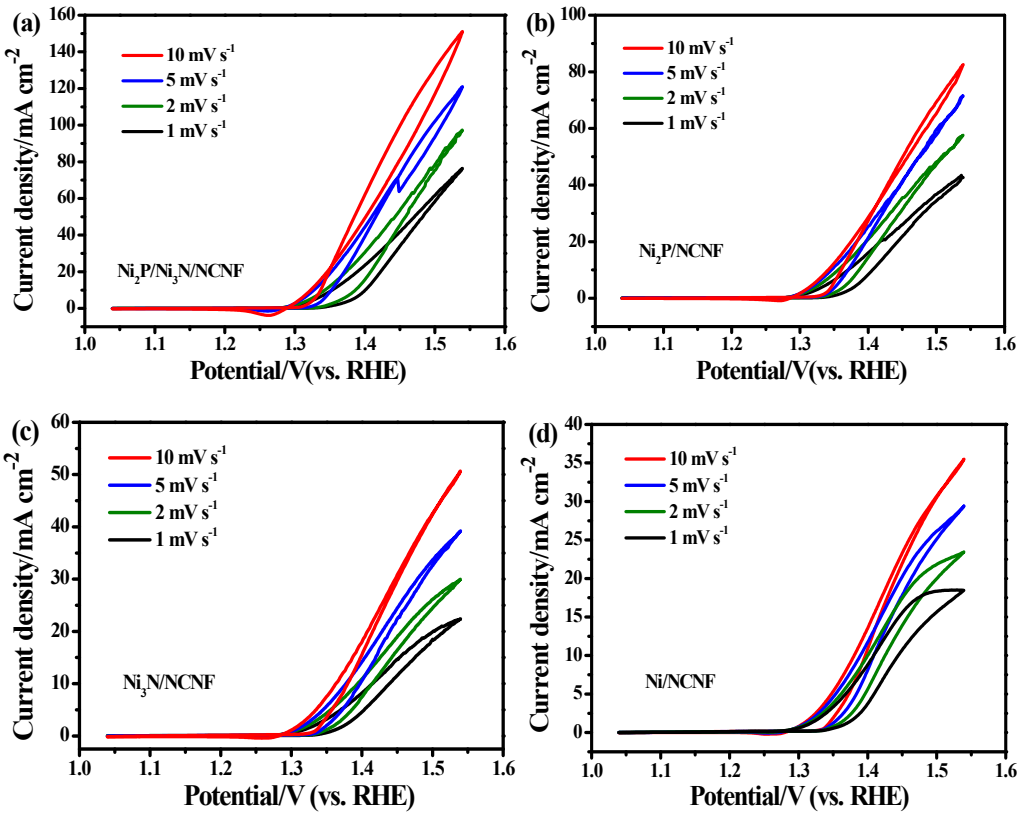

Fig. S10. CV curves in 1 M KOH solution with 0.33 M urea at different scan rates of 1, 2, 5, and 10 mV s^{-1} for (a) Ni_2P/Ni_3N/NCNF, (b) Ni_2P/NCNF, (c) Ni_3N/NCNF, and (d) Ni/NCNF.

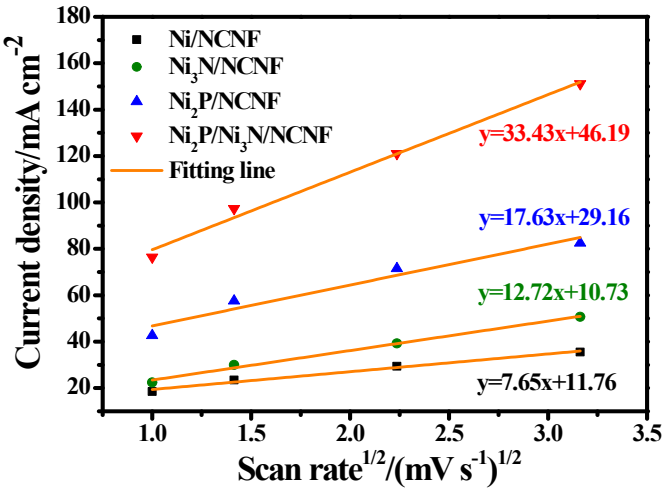

Fig. S11. The plot of peak current density vs. the square root of scan rate for all the samples.

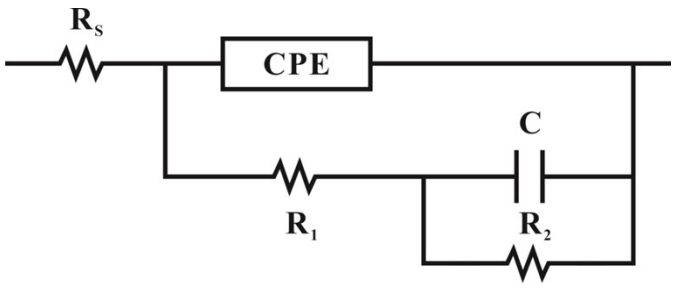

Fig. S12. The equivalent circuit used in EIS fitting for UOR.

R_s is a sign of the uncompensated solution resistance, CPE is a constant phase element, R_1 reflects the charge-transfer resistance, C and R_2 represent the pseudocapacitance and the resistance of the reconstruction of the surface of the catalysts.

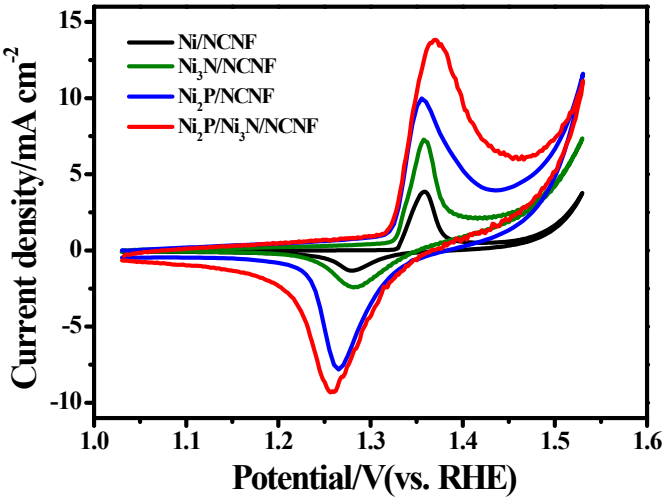

Fig. S13. Cyclic voltammetry curves measured in 1 M KOH at a scan rate of 10 mV s^{-1} for all samples.

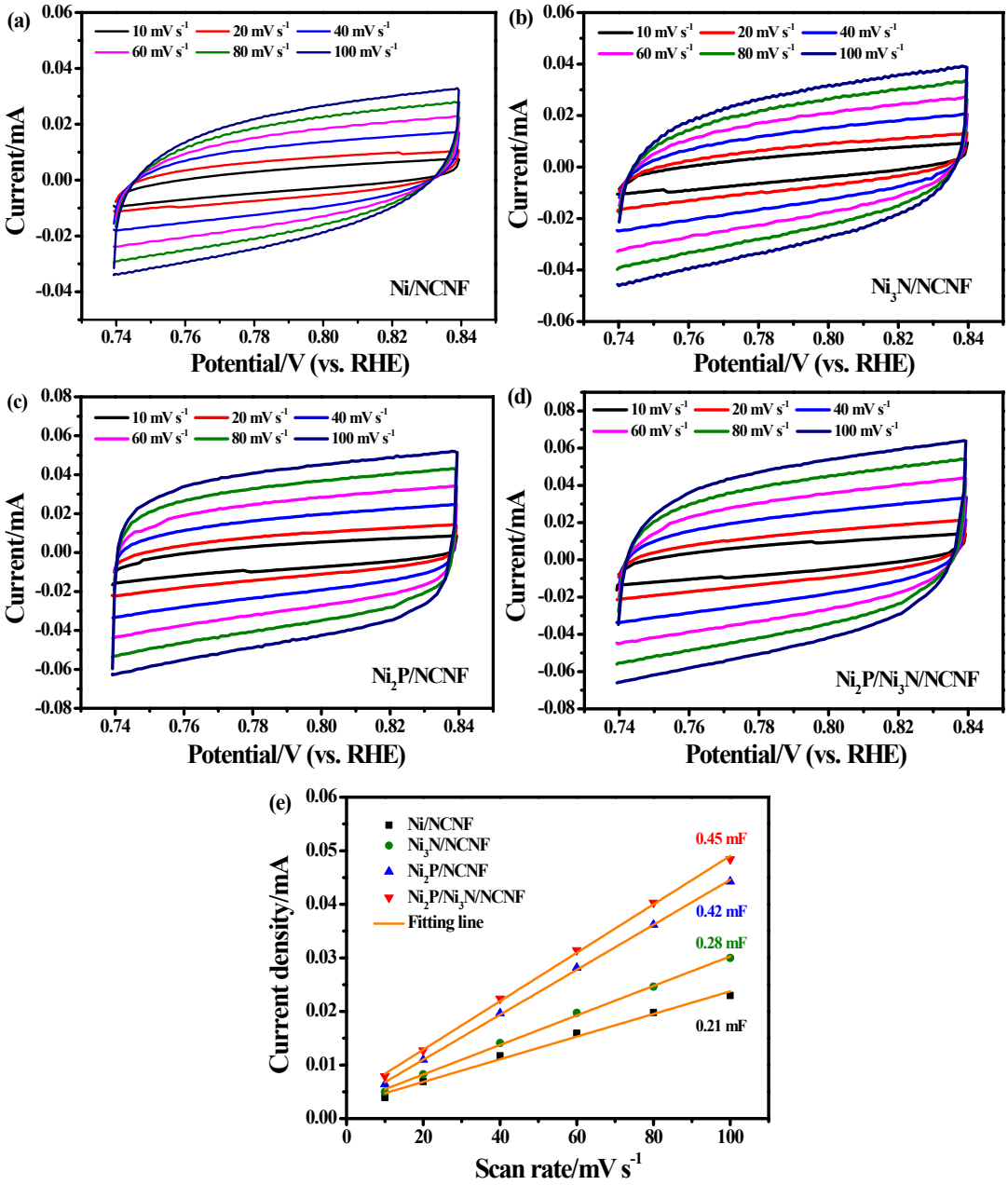

Fig. S14. Cyclic voltammograms of (a) Ni/NCNF, (b) Ni_3N/NCNF, (c) Ni_2P/NCNF, and (d) Ni_2P/ Ni_3N/NCNF at different scan rates of 10, 20, 40, 60, 80, and 100 mV s^{-1}. (e) Scan rate dependence of the current derived from double-layer capacitance measurements of Ni/NCNF, Ni_3N/NCNF, Ni_2P/NCNF, and Ni_2P/ Ni_3N/NCNF.

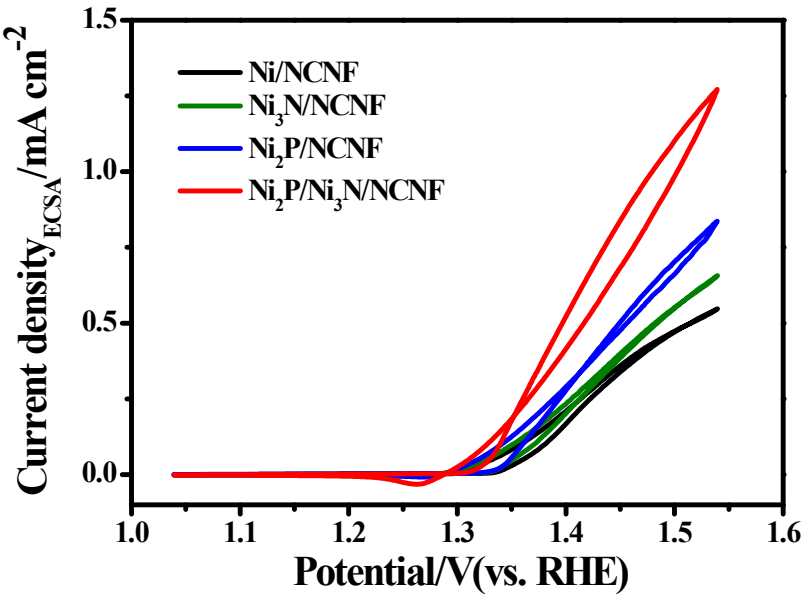

Fig. S15. Specific activity of Ni/NCNF, Ni_3N/NCNF, Ni_2P/NCNF, and Ni_2P/Ni_3N/NCNF catalysts in 1 M KOH with 0.33 M urea at a scan rate of 10 mV s^{-1}.

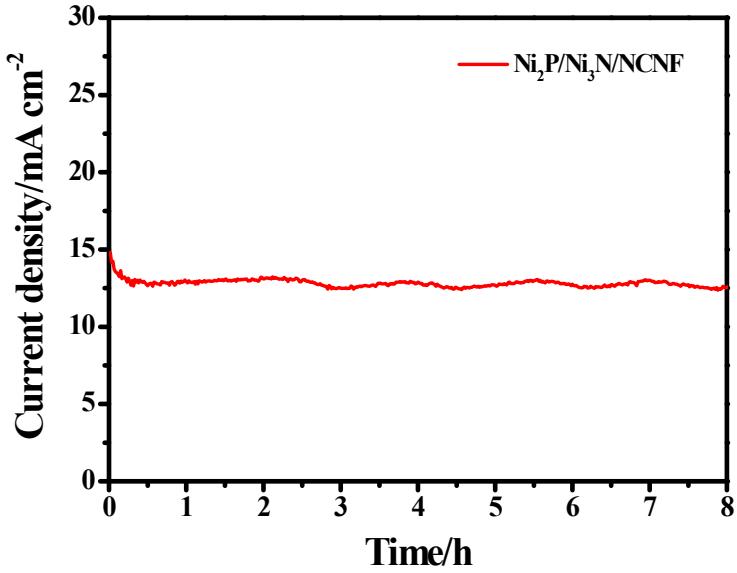

Fig. S16. A CA curve of Ni_2P/Ni_3N/NCNF for 8 h.

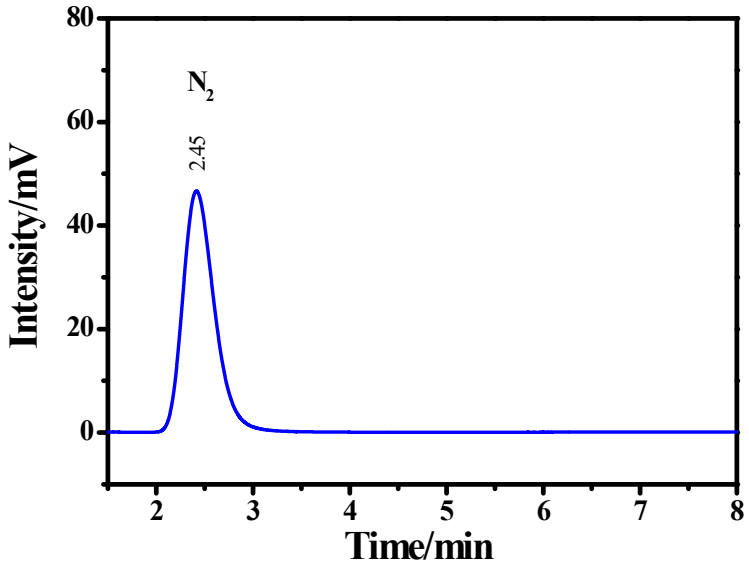

Fig. S17. The gas chromatography spectrum of the N_2 product.

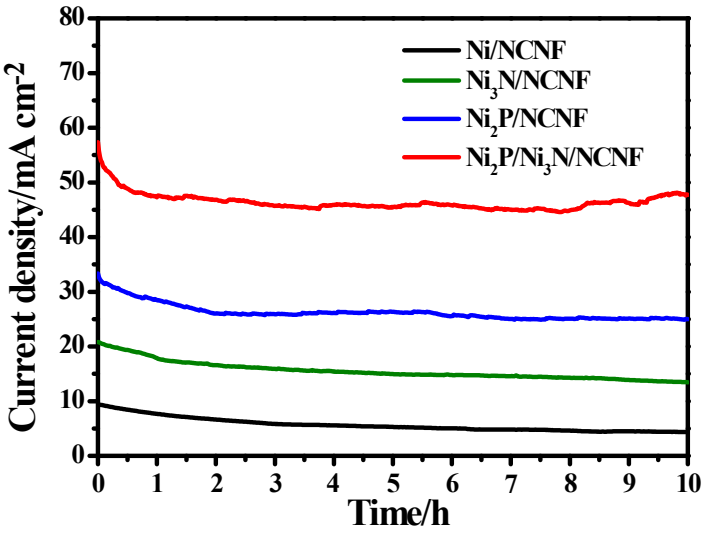

Fig. S18. CA curves of Ni/NCNF, Ni_3N/NCNF, Ni_2P/NCNF, and Ni_2P/Ni_3N/NCNF.

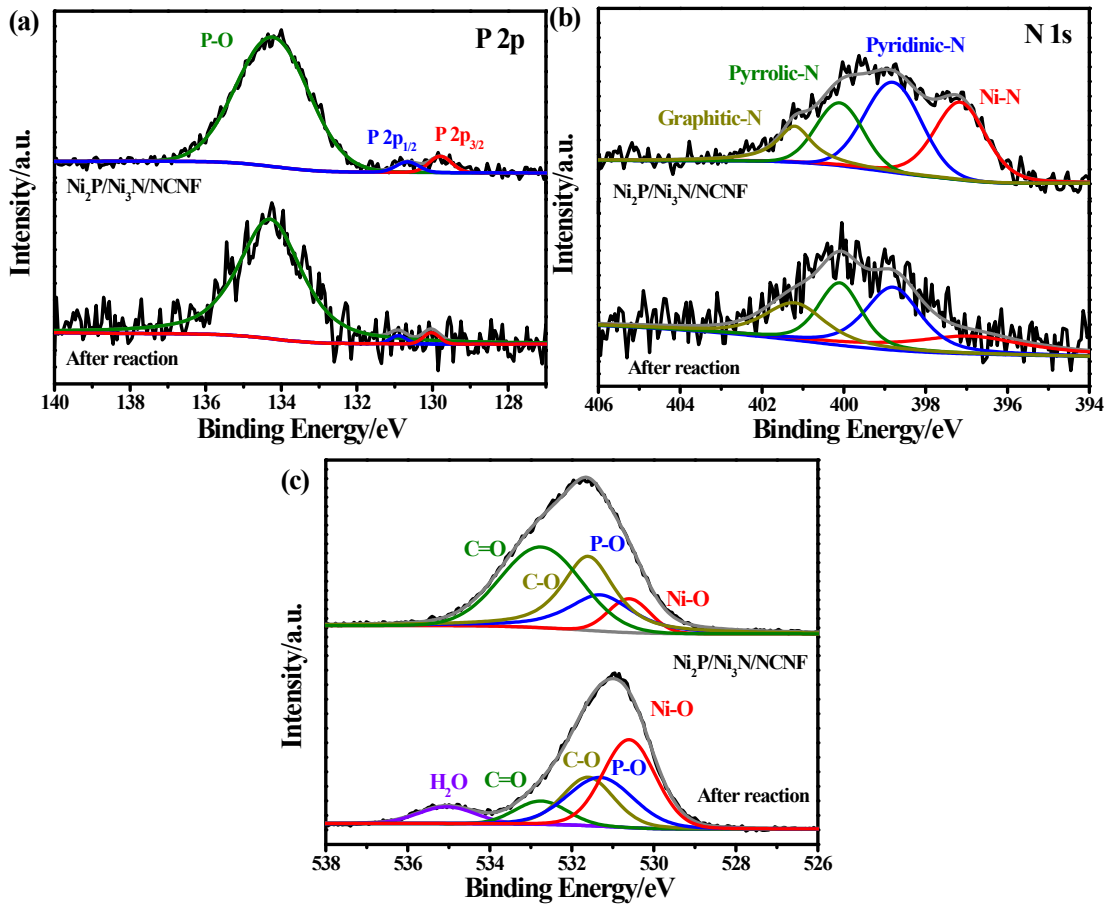

Fig. S19. The XPS spectra of (a) P 2p, (b) N 1s, and (c) O 1s of Ni_2P/Ni_3N/NCNF before and after urea electrolysis.

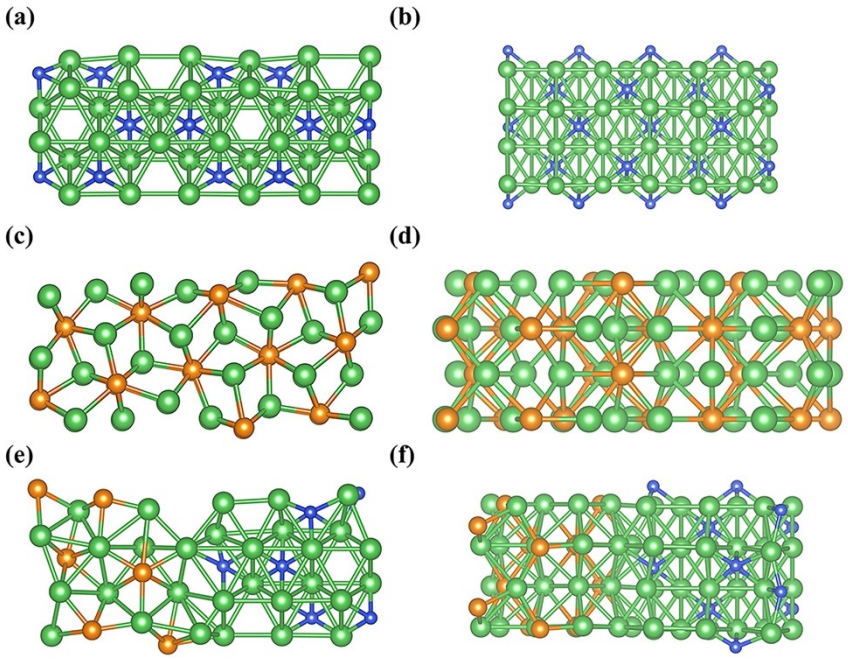

Fig. S20. The structural models of Ni_3N (a, b), Ni_2P (c, d), and Ni_2P/Ni_3N (e, f).

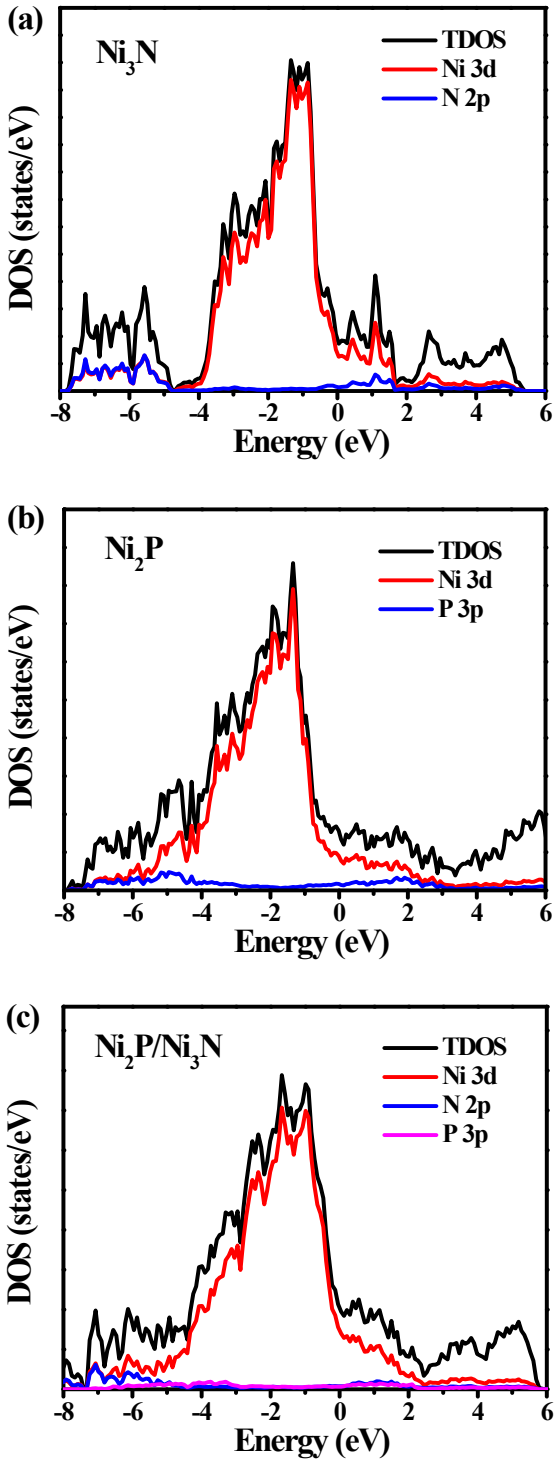

Fig. S21. The total density of the states (TDOS) of (a) Ni_3N, (b) Ni_2P, and (c) Ni_2P/Ni_3N.

Table S1. Structural parameters of Ni_2P and Ni_3N in Ni_2P/Ni_3N/NCNF derived from the Rietveld refinement.

Phase	Ni_2P^E	Ni_2P^S	Ni_3N^E	Ni_3N^S
Cell length a	5.8608	5.859	4.6230	4.621
Cell length b	5.8608	5.859	4.6230	4.621
Cell length c	3.3846	3.382	4.3053	4.304
Cell angle alpha	90	90	90	90
Cell angle beta	90	90	90	90
Cell angle gamma	120	120	120	120
Cell volume	100.681	100.5	79.685	79.6
Crystal density	7.3415	7.351	7.9022	7.91
Space group	P-62m	P-62m	P6322	P6322

E: Experimental S: Standard

Table S2. Element composition of Ni_2P/Ni_3N/NCNF based on the EDX.

Element	Weight %	Atomic %
C	76.02	87.45
N	3.21	3.16
O	6.36	5.49
P	2.33	1.04
Ni	12.06	2.83

Table S3. The binding energy of Ni 2p for Ni/NCNF, Ni_3N/NCNF, Ni_2P/NCNF, and Ni_2P/Ni_3N/NCNF.

Catalysts	Binding energy/eV					
	Ni $2p_{3/2}$			Ni $2p_{1/2}$		
	Ni^0	Ni^{2+}	Satellite	Ni^0	Ni^{2+}	Satellite
Ni/NCNF	852.35	854.88	860.19	869.95	872.48	878.99
Ni_3N/NCNF	852.45	855.48	860.02	870.05	873.08	879.39
Ni_2P/NCNF	853.14	856.73	861.37	870.74	874.33	879.71
Ni_2P/Ni_3N/NCNF	853.24	856.75	861.83	870.84	874.35	880.44

Table S4. The binding energy of P 2p for Ni_2P/NCNF and Ni_2P/Ni_3N/NCNF.

Catalysts	Binding energy/eV		
	P-O	P $2p_{1/2}$	P $2p_{3/2}$
Ni_2P/NCNF	134.12	130.19	129.32
Ni_2P/Ni_3N/NCNF	134.23	130.66	129.79

Table S5. The binding energy of N 1s for Ni/NCNF, Ni_3N/NCNF, Ni_2P/NCNF, and Ni_2P/Ni_3N/NCNF.

Catalysts	Binding energy/eV			
	pyridinic-N	pyrrolic-N	graphitic-N	Ni-N
Ni/NCNF	398.80	400.10	401.20	/
Ni_3N/NCNF	398.80	400.10	401.20	397.85
Ni_2P/NCNF	398.80	400.10	401.20	/
Ni_2P/Ni_3N/NCNF	398.80	400.10	401.20	397.62

Table S6. The binding energy of O 1s for Ni/NCNF, Ni_3N/NCNF, Ni_2P/NCNF, and Ni_2P/Ni_3N/NCNF.

Catalysts	Binding energy/eV			
	Ni-O	C-O	C=O	P-O
Ni/NCNF	530.60	531.60	532.75	/
Ni_3N/NCNF	530.60	531.60	532.75	/
Ni_2P/NCNF	530.60	531.60	532.75	531.30
Ni_2P/Ni_3N/NCNF	530.60	531.60	532.75	531.30

Table S7. The onset potential, redox potential of Ni^{2+}/Ni^{3+}, and the overpotential at 10 mA cm^{-2} of the as-prepared catalysts for OER.

Catalyst	Onset potential/V vs. RHE	Redox potential of Ni^{2+}/Ni^{3+}/V vs. RHE	Overpotential at 10 mA cm^{-2}/mV
Ni_2P/Ni_3N/NCNF	1.316	1.362	283
Ni_2P/NCNF	1.320	1.361	311
Ni_3N/NCNF	1.326	1.378	334
Ni/NCNF	1.332	1.379	359

Table S8. EIS fitting parameters from equivalent circuit for OER.

Catalysts	R_s/Ω	CPE/S s^{-n}	n/0<n<1	R_{ct}/Ω
Ni/NCNF	6.986	1.398E-004	0.77	206.20
Ni_3N/NCNF	7.051	1.234E-004	0.81	137.10
Ni_2P/NCNF	9.283	1.454E-003	0.93	99.12
Ni_2P/Ni_3N/NCNF	7.177	1.177E-004	0.87	64.37

Table S9. The comparison of the catalytic properties of Ni-based catalysts for UOR in recent years

Catalyst	Electrolyte	Scan rate/mV s^{-1}	Potential at 10 mA cm^{-2}/V	Ref.
a-Ni_2P/G	1 M KOH+0.5 M urea	5	1.28 V vs. RHE	[11]
$MoNi_4/MoO_x$@NF	1 M KOH+0.33 M urea	10	1.29 V vs. RHE	[12]
NiS@$Ni_3S_2/NiMoO_4$	1 M KOH+0.5 M urea	2	1.30 V vs. RHE	[13]
$Ni(OH)_2$-NSs/CC	1 M KOH+0.5 M urea	5	1.32 V vs. RHE	[14]
P-NF	1 M KOH+0.33 M urea	5	1.32 V vs. RHE	[15]
Ni@C-V_2O_3/NF	1 M KOH+0.5 M urea	5	1.32 V vs. RHE	[16]
Mo-doped Ni_3S_2	1 M KOH+0.3 M urea	2	1.33 V vs. RHE	[17]
$NiSe_2$-NiO 350	1 M KOH+0.33 M urea	10	1.33 V vs. RHE	[18]
NP-$Ni_{0.7}Fe_{0.3}$ Ni foam	1 M KOH+0.33 M urea	5	1.33 V vs. RHE	[19]
Ni_2P/Ni_3N/NCNF	**1 M KOH+0.33 M urea**	**10**	**1.337 V vs. RHE**	**This work**
Ni_3S_2/MWCNTs/NF	1 M KOH+0.5 M urea	5	1.338 V vs. RHE	[20]
Cu_2S@Ni_3Se_2	1 M KOH+0.5 M urea	5	1.338 V vs. RHE	[21]
Ni_4N/Cu_3N	1 M KOH+0.5 M urea	5	1.34 V vs. RHE	[22]
Ni_3N-350/NF	1 M KOH+0.5 M urea	5	1.34 V vs. RHE	[23]
Ni_3N/rGO@NF-350	1 M KOH+0.5 M urea	5	1.342 V vs. RHE	[24]
MNPBA-P	1 M KOH+0.5 M urea	20	1.344 V vs. RHE	[25]
$Ni/Ni_{0.2}Mo_{0.8}N/MoO_3$	1 M KOH+0.5 M urea	2	1.349 V vs. RHE	[26]
$Ni(OH)_2$@NF	1 M KOH+0.33 M urea	5	1.35 V vs. RHE	[27]
Ni_3N NA/CC	1 M KOH+0.33 M urea	5	1.35 V vs. RHE	[28]
Ni/NiO@NC	1 M KOH+0.33 M urea	5	1.35 V vs. RHE	[29]
$Ni_{0.85}Se$/rGO	1 M KOH+0.5 M urea	5	1.36 V vs. RHE	[30]
$NiSe_2$	1 M KOH+0.33 M urea	5	1.36 V vs. RHE	[31]
NiF_3/Ni_2P@CC-2	1 M KOH+0.33 M urea	10	1.36 V vs. RHE	[32]
Ni_2P/Fe_2P/NF	1 M KOH+0.5 M urea	10	1.36 V vs. RHE	[33]
Ni-Mo nanotube	1 M KOH+0.1 M urea	5	1.36 V vs. RHE	[34]
Ni-MOF	1 M KOH+0.33 M urea	10	1.36 V vs. RHE	[35]
V–Ni_3N/NF	1 M KOH+0.5 M urea	2	1.361 V vs. RHE	[36]
NiFe hollow cages	1 M KOH+0.5 M urea	5	1.37 V vs. RHE	[37]
NiFeMo	1 M KOH+0.33 M urea	5	1.38 V vs. RHE	[38]
Ni_3Se_4	1 M KOH+0.1 M urea	5	1.38 V vs. RHE	[39]
Ni-MOF-0.5	1 M KOH+0.5 M urea	5	1.381 V vs. RHE	[40]
Ni/SiO_x/N-C	1 M KOH+0.33 M urea	5	1.384 V vs. RHE	[41]
β-NiS	1 M KOH+0.33 M urea	5	1.4 V vs. RHE	[42]

Table S10. EIS fitting parameters from equivalent circuit for UOR.

Catalysts	R_s/Ω	CPE/S s^{-n}	n/0<n<1	R_{ct}/Ω	C/mF	R_2/Ω
Ni/NCNF	8.529	3.854E-005	0.59	109.02	3.541E-005	29.94
Ni_3N/NCNF	9.584	5.278E-004	0.76	88.98	1.135E-004	24.37
Ni_2P/NCNF	9.495	6.124E-004	0.58	65.13	1.456E-004	15.15
Ni_2P/Ni_3N/NCNF	5.247	3.358E-004	0.84	45.24	4.286E-003	7.18

Table S11.The comparison of the calculated ECSA from the method of C_{dl} and reduction peak integration.

ECSA/cm^{-2}	Reduction peak integration method	C_{dl} method
Ni/NCNF	4.54	5.25
Ni_3N/NCNF	5.40	7.00
Ni_2P/NCNF	6.91	10.50
Ni_2P/Ni_3N/NCNF	8.32	11.25

Table S12. The comparison of the catalytic properties of Ni-based heterostructure catalysts for urea-assisted water splitting in two electrode system in recent years.

Catalyst	Potential at 10 mA cm^{-2} for urea electrolysis/V	Potential at 10 mA cm^{-2} for water splitting /V	Ref.
$Ni/Ni_{0.2}Mo_{0.8}N/MoO_3$	1.356	1.520	[26]
$Ni\text{-}NiO\text{-}Mo_{0.84}Ni_{0.16}/NF$	1.37	1.52	[43]
$(Ni\text{-}WO_2)@C/NF$	1.38	1.56	[44]
$Ni_2P/Ni_3N/NCNF$	**1.39**	**1.59**	**This work**
$NiSe_2\text{-}NiO$ 350	1.39	1.60	[18]
$NiS@Ni_3S_2/NiMoO_4$	1.40	1.60	[13]
$NiS_2\text{-}MoS_2$	1.40	1.63	[45]
$NiS/MoS_2@FCP$	1.42	1.72	[46]
$CoN/Ni(OH)_2$	1.43	1.64	[47]
$Ni_4N/Cu_3N/CF$	1.48	1.67	[22]
$Cu_2S@Ni_3Se_2$	1.48	1.70	[21]
Ni_2P/Fe_2P	1.50	1.58	[25]
$NiF_3/Ni_2P@CC\text{-}2$	1.54	1.58	[32]
$N\text{-}NiS/NiS_2$	1.62	1.74	[48]
NiF_2/Ni_2P	1.5@40 mA cm^{-2}	1.8@40 mA cm^{-2}	[49]
$Ni@C\text{-}V_2O_3/NF$	1.46@50 mA cm^{-2}	1.66@50 mA cm^{-2}	[16]

Table S13. Element composition of Ni_2P/Ni_3N/NCNF based on the EDX after stability test.

Element	Weight %	Atomic %
C	69.79	82.46
N	3.44	3.49
O	11.03	9.80
P	0.95	0.43
Ni	12.75	3.08
K	2.04	0.74

References

1. Y. H. Fang and Z. P. Liu, *ACS Catal.*, 2014, **4**, 4364-4376.
2. N. Kakati, J. Maiti, K. S. Lee, B. Viswanathan and Y. S. Yoon, *Electrochim. Acta*, 2017, **240**, 175-185.
3. D. Yang, Y. Gu, X. Yu, Z. Lin, H. Xue and L. Feng, *ChemElectroChem*, 2018, **5**, 659-664.
4. J. Chen, H. Li, Z. Pei, Q. Huang, Z. Yuan, C. Wang, X. Liao, G. Henkelman, Y. Chen and L. Wei, *J. Mater. Chem. A*, 2020, **8**, 15951-15961.
5. Z. Liu, D. Liu, L. Zhao, J. Tian, J. Yang and L. Feng, *J. Mater. Chem. A*, 2021, **9**, 7750-7758.
6. G. Kresse and J. Furthmüller, *Comput. Mater. Sci.*, 1996, **6**, 15-50.
7. G. Kresse and J. Furthmüller, *Phys. Rev. B*, 1996, **54**, 11169-11186.
8. J. P. Perdew, K. Burke and M. Ernzerhof, *Phys. Rev. Lett.*, 1996, **77**, 3865-3868.
9. G. Kresse and D. Joubert, *Phys. Rev. B*, 1999, **59**, 1758-1775.
10. H. J. Monkhorst and J. D. Pack, *Phys. Rev. B*, 1976, **13**, 5188-5192.
11. Y. Tong, L. Chen, P. J. Dyson and Z. Fei, *J. Mater. Sci.*, 2021, **56**, 17709-17720.
12. L. Meng, L. Li, J. Wang, S. Fu, Y. Zhang, J. Li, C. Xue, Y. Wei and G. Li, *Electrochim. Acta*, 2020, **350**, 136382.
13. L. Sha, T. Liu, K. Ye, K. Zhu, J. Yan, J. Yin, G. Wang and D. Cao, *J. Mater. Chem. A*, 2020, **8**, 18055-18063.
14. J. Chen, S. Ci, G. Wang, N. Senthilkumar, M. Zhang, Q. Xu and Z. Wen, *ChemElectroChem*, 2019, **6**, 5313-5320.
15. L. Fei, H. Sun, R. Ran, W. Zhou and Z. Shao, *Ind. Eng. Chem. Res.*, 2021, **60**, 1185-1193.
16. G. Qian, J. Chen, L. Luo, H. Zhang, W. Chen, Z. Gao, S. Yin and P. Tsiakaras, *ACS Appl. Mater. Inter.*, 2020, **12**, 38061-38069.
17. H. Xu, Y. Liao, Z. Gao, Y. Qing, Y. Wu and L. Xia, *J. Mater. Chem. A*, 2021, **9**, 3418-3426.
18. Z. Liu, C. Zhang, H. Liu and L. Feng, *Appl. Catal. B-Environ*, 2020, **276**, 119165.
19. Z. Cao, T. Zhou, X. Ma, Y. Shen, Q. Deng, W. Zhang and Y. Zhao, *ACS Sustain. Chem. Eng.*, 2020, **8**, 11007-11015.
20. Z. Zhao, L. Yang, Z. Wang, L. Wang, G. Guo, J. Chen, Y. Li, C. Wang, J. Zhao and Z. Cai, *J. Electrochem. Soc.*, 2020, **167**, 126514.
21. L. Lv, Z. Li, H. Wan and C. Wang, *J. Colloid Interf. Sci.*, 2021, **592**, 13-21.
22. J. Li, C. Yao, X. Kong, Z. Li, M. Jiang, F. Zhang and X. Lei, *ACS Sustain. Chem. Eng.*, 2019, **7**, 13278-13285.
23. Z. Zhao, J. Zhao, H. Wang, X. Li, L. Yang, Z. Zhao, X. Liu, Y. Liu, P. Liu and Z. Cai, *Int. J. Hydrogen. Energ.*, 2020, **45**, 14199-14207.
24. F. Wang, D. Zhao, L. Zhang, L. Fan, X. Zhang and S. Hu, *Nanomaterials (Basel)*, 2019, **9**, 1583.
25. H. Xu, K. Ye, K. Zhu, Y. Gao, J. Yin, J. Yan, G. Wang and D. Cao, *ACS Sustain. Chem. Eng.*, 2020, **8**, 16037-16045.
26. R.-Q. Li, S. Li, M. Lu, Y. Shi, K. Qu and Y. Zhu, *J. Colloid Interf. Sci.*, 2020, **571**, 48-54.
27. L. Xia, Y. Liao, Y. Qing, H. Xu, Z. Gao, W. Li and Y. Wu, *ACS Appl. Energ. Mater.*, 2020, **3**, 2996-3004.
28. Q. Liu, L. Xie, F. Qu, Z. Liu, G. Du, A. M. Asiri and X. Sun, *Inorg. Chem. Front.*, 2017, **4**, 1120-1124.
29. X. Ji, Y. Zhang, Z. Ma and Y. Qiu, *ChemSusChem*, 2020, **13**, 5004-5014.
30. L. Zhao, Y. Chang, M. Jia, J. Jia and Z. Wen, *J. Alloy. Compd.*, 2021, **852**, 156751.

31. P. Xiong, X. Ao, J. Chen, J.-G. Li, L. Lv, Z. Li, M. Zondode, X. Xue, Y. Lan and C. Wang, *Electrochim. Acta*, 2019, **297**, 833-841.
32. K. Wang, W. Huang, Q. Cao, Y. Zhao, X. Sun, R. Ding, W. Lin, E. Liu and P. Gao, *Chem. Eng. J.*, 2022, **427**, 130865.
33. L. Yan, Y. Sun, E. Hu, J. Ning, Y. Zhong, Z. Zhang and Y. Hu, *J. Colloid Interf. Sci.*, 2019, **541**, 279-286.
34. J. Zhang, T. He, M. Wang, R. Qi, Y. Yan, Z. Dong, H. Liu, H. Wang and B. Y. Xia, *Nano Energy*, 2019, **60**, 894-902.
35. D. Zhu, C. Guo, J. Liu, L. Wang, Y. Du and S.-Z. Qiao, *Chem. Commun.*, 2017, **53**, 10906-10909.
36. R.-Q. Li, Q. Liu, Y. Zhou, M. Lu, J. Hou, K. Qu, Y. Zhu and O. Fontaine, *J. Mater. Chem. A*, 2021, **9**, 4159-4166.
37. Y. Feng, X. Wang, P. Dong, J. Li, L. Feng, J. Huang, L. Cao, L. Feng, K. Kajiyoshi and C. Wang, *Sci. Rep.*, 2019, **9**, 15965.
38. Z. Lv, Z. Li, X. Tan, Z. Li, R. Wang, M. Wen, X. Liu, G. Wang, G. Xie and L. Jiang, *Appl. Surf. Sci.*, 2021, **552**, 149514.
39. J.-Y. Zhang, X. Tian, T. He, S. Zaman, M. Miao, Y. Yan, K. Qi, Z. Dong, H. Liu and B. Y. Xia, *J. Mater. Chem. A*, 2018, **6**, 15653-15658.
40. S. Zheng, Y. Zheng, H. Xue and H. Pang, *Chem. Eng. J.*, 2020, **395**, 125166.
41. M. Yuan, X. Guo, N. Li and H. Pang, *J. Colloid Interf. Sci.*, 2021, **589**, 56-64.
42. T.-H. Wu, Y.-C. Lin, B.-W. Hou and W.-Y. Liang, *Catalysts*, 2020, **10**, 1280.
43. Q. Xu, G. Qian, S. Yin, C. Yu, W. Chen, T. Yu, L. Luo, Y. Xia and P. Tsiakaras, *ACS Sustain. Chem. Eng.*, 2020, **8**, 7174-7181.
44. F. Shen, W. Jiang, G. Qian, W. Chen, H. Zhang, L. Luo and S. Yin, *J. Power. Sources*, 2020, **458**, 228014.
45. S. Wang, L. Zhao, J. Li, X. Tian, X. Wu and L. Feng, *J. Energy Chem.*, 2022, **66**, 483-492.
46. Y. Zheng, P. Tang, X. Xu and X. Sang, *J. Solid State Chem.*, 2020, **292**, 121644.
47. Y. Cheng, F. Liao, H. Dong, H. Wei, H. Geng and M. Shao, *J. Power. Sources*, 2020, **480**, 229151.
48. H. Liu, Z. Liu, F. Wang and L. Feng, *Chem. Eng. J.*, 2020, **397**, 125507.
49. H. Liu, Z. Liu and L. Feng, *Nanoscale*, 2019, **11**, 16017-16025.